International Journal of Thin Films Science and Technology

http://dx.doi.org/10.18576/ijtfst/160101

Exact Solutions of the Telecommunication Model via the Extended Generalized Riccati Equation Mapping Method

Mohamed Hafez[1], *Ali Akgül*[2,3,*], *Farrah Ashraf*[4], *Saliha Manzoor*[5], *and Romana Ashraf*[4]

[1] Faculty of Engineering and Quantity Surveying, INTI International University Colleges, Nilai, Malaysia
[2] Department of Electronics and Communication Engineering, Saveetha School of Engineering, SIMATS, Chennai, Tamilnadu, India
[3] Department of Mathematics, Art and Science Faculty, Siirt University, 56100 Siirt, Türkiye
[4] Department of Computer Science & IT, The University of Lahore, Lahore, Pakistan
[5] Department of Mathematics and Statistics, The University of Lahore, Lahore, Pakistan

Received: 22 Sep. 2026, Revised: 2 Oct. 0226, Accepted: 2 Nov. 2026
Published online: 1 Jan. 2027

Abstract: In this research, we obtain exact soliton solutions for the (2+1)-dimensional nonlinear telecommunication equation by using the extended generalized Riccati equation mapping approach. Numerous innovative solutions have been discovered. The solutions discovered by the present approach are diverse in nature and comprise bright, dark, singular, periodic and rational solutions. We demonstrate that the existence of these solutions depends upon the network's parameters. We compare our new results with the established results. Information can also be transmitted through optical fibers using the solutions presented here. Most of the obtained results are generated for the first time. Furthermore, the solutions demonstrate that the novel techniques are remarkably straightforward, unambiguous, productive, and successful. They may also be used for a variety of other nonlinear partial differential equations (NLPDEs), which describe various dynamical aspects of other wave models.

Keywords: The nonlinear telecommunication model; Bright wave; Dark wave; Periodic wave; Rational wave; the extended generalized Riccati equation mapping method.

1 Introduction

Nonlinear evolution models (NLEM) have been applied to a wide range of nonlinear phenomena, including water waves, ion-acoustic waves, fiber optics, microwave physics, non-Newtonian turbulent flows, and more [1, 2]. For the purpose of comprehending and improving current communication systems, nonlinear telecommunication models are crucial. These models take into consideration the nonlinear behaviours displayed by different parts of a communication network, including signal processors, amplifiers, and optical fibers.

Using the information gathered about the wave profile, certain techniques, particularly the neural network technique [3], sine-Gordon and improved Bernoulli sub-equation expansion [4], finite difference [5], the Pfaffian technique [6], Lie-Bäcklund symmetries [7], the variable separation method [8], Jacobi elliptic function expansion [9, 10], the exponential function method [11], the extended $\left(\frac{G'}{G}\right)$-expansion [12], double Wronskian [13], the resilient Hirota bilinear method [14], the nonlinear capacity method [15] and the unified scheme [16], several outcomes that are analogous to (NLEM) have been derived and published in the literature. An extensive discussion of the (3+1)-dimensional Boiti-Leon-Manna-Pempinelli equation may be found in [17]. In [18], a handy technique has been presented. The stability analysis of the fourth-order iterative method has been studied by Cordero et al. in [19]. Numerous studies have been conducted on the classical Boussinesq equations in [20]. A discrete normal vector field approximation using time scale calculus has been proposed in [21]. In [22], traveling wave solutions of the nonlinear Klein-Gordon equation were discovered; see also [23, 24]. The most effective methods for obtaining analytical solutions of complicated nonlinear models are bifurcation analysis along with dynamical systems. A crucial method for obtaining precise analytical solutions of complicated nonlinear models of the Hamiltonian system is bifurcation analysis

* Corresponding author e-mail: aliakgul00727@gmail.com

© 2027 NSP
Natural Sciences Publishing Cor.

and the dynamical system, which has extensive applications to a variety of models, including [25].
It is possible to construct more effective and dependable communication systems by using nonlinear models, which are significant because of their capacity to describe real-world conditions more correctly. For example, in the field of optical communications, the nonlinear optical phenomenon known as the Kerr effect can alter the fiber's refractive index, which can have an impact on signal propagation. Similarly, in wireless communications, where power amplifiers are used, nonlinear characteristics can cause distortions and lower the quality of transmitted signals.
To extract the model's many nonlinear dynamical natures, researchers have put in a great deal of effort. Baskonus et al. [26] acquired dark, complex and trigonometric function solutions using the tanh function method. By using three distinct techniques, namely the Kudryashov, the fractional linear transform, and the simplest equation methods, Kumar and El-Ganaini [27] were able to construct traveling and solitary wave solutions. Through the use of the Jacobi elliptic function expansion technique, Zayed found Jacobi elliptic and soliton solutions [28]. Sardar et al. [29] developed three integral schemes, namely the $\left(\frac{G'}{G}\right)$-expansion, sine-cosine and extended tanh methods, to produce multiple travelling wave solutions. Numerous other researchers have studied the model using different approaches.
The article is organized as follows. To find the wave equation associated with the telecommunication model, we apply the proper wave transformation in Section 2. The algorithm of the extended generalized Riccati equation mapping method is given in Section 3, and its essential components exhibit multiple solutions. The solution of the nonlinear telecommunication model using the proposed approach is shown in Section 4. Section 5 presents various kinds of graphical representations that help in the visualization of the research outcomes. The physical explanation of the observed results is presented in Section 6. In Section 7, the noteworthy findings of the study are outlined.

2 The mathematical analysis of the nonlinear telecommunication model

The nonlinear telecommunication model is given by [26, 28, 29]

$$\frac{\partial^2}{\partial t^2}\left(U-\alpha U^2+\beta U^3\right)-\gamma_0^2\delta_1^2 U_{xx} - \frac{\gamma_0^2\delta_1^4}{12}U_{xxxx}-\rho_0^2\delta_2^2 U_{yy} - \frac{\rho_0^2\delta_2^4}{12}U_{yyyy}=0, \quad (2.1)$$

where $U=U(x,y,t)$ represents the voltage present in the transmission lines, x and y are spatial distances, and t is the temporal variable. α and β are nontrivial constants. The longitudinal distance δ_1 is the space between two adjacent parts, while the transverse distance δ_2 is the space between two adjacent sections. In order to transform the model equation into an ordinary differential equation (ODE), we consider the traveling wave transformation

$$U=Q(\zeta), \quad (2.2)$$

$$\zeta=k(x+y-ht), \quad (2.3)$$

where k and h are nonzero real or complex constants. Inserting Eq. (2.2) and Eq. (2.3) into Eq. (2.1) and dividing by k^2 gives

$$h^2\left(Q-\alpha Q^2+\beta Q^3\right)_{\zeta\zeta} - \left(\gamma_0{}^2\delta_1{}^2+\rho_0{}^2\delta_2{}^2\right)Q_{\zeta\zeta} - \frac{k^2}{12}\left(\gamma_0^2\delta_1^4+\rho_0^2\delta_2^4\right)Q_{\zeta\zeta\zeta\zeta}=0. \quad (2.4)$$

Integrating Eq. (2.4) twice with respect to ζ and setting the integration constants to zero, we obtain

$$12\left(h^2-\gamma_0{}^2\delta_1{}^2-\rho_0{}^2\delta_2{}^2\right)Q(\zeta) - 12h^2\alpha Q(\zeta)^2+12h^2\beta Q(\zeta)^3 - k^2\left(\gamma_0{}^2\delta_1{}^4+\rho_0{}^2\delta_2{}^4\right)Q''(\zeta)=0. \quad (2.5)$$

3 Algorithm of the extended generalized Riccati equation mapping method

Consider a nonlinear partial differential equation in the dependent variable U and the independent variables $x=(x_0=t,x_1,x_2,\ldots,x_m)$:

$$E\left(U,U_t,U_{x_i},U_{x_ix_j},\cdots\right)=0, \quad (3.1)$$

where E is usually a polynomial function of its arguments, and the partial derivatives are denoted by subscripts. The main steps of the method are as follows.
Step 1. Consider the traveling wave transformation

$$U(x,y,t)=Q(\zeta), \quad \zeta=k(x+y-ht). \quad (3.2)$$

Using Eq. (3.2), we can convert Eq. (3.1) into an ordinary differential equation for $R(\zeta)$,

$$R\left(Q,Q',Q'',\cdots\right)=0, \quad (3.3)$$

where primes denote ordinary derivatives with respect to ζ.
Step 2. Integrate Eq. (3.3) one or more times, whenever possible, which yields integration constants. For simplicity, the integration constants may be taken to be zero.

© 2027 NSP
Natural Sciences Publishing Cor.

Step 3. Assume that Eq. (3.3) has a formal solution of the form [30–32]

$$Q(\zeta)=\sum_{j=0}^{n}A_j\left(\frac{G'(\zeta)}{G(\zeta)}\right)^j, \tag{3.4}$$

where $A_j\,(j=0,1,\ldots,n)$ are constants with $A_n\neq 0$, and $G=G(\zeta)$ solves the generalized Riccati equation

$$G'(\zeta)=\sigma+\rho G(\zeta)+\lambda G^2(\zeta), \tag{3.5}$$

in which σ,ρ and λ are real constants and $\lambda\neq 0$.

Step 4. Determine the positive integer n by the homogeneous balance between the highest-order derivative and the nonlinear terms in Eq. (3.3).

Step 5. Substitute Eq. (3.4) together with Eq. (3.5) into Eq. (3.3), collect all coefficients of $G^j(\zeta)$ $(j=0,\pm1,\pm2,\cdots)$, and set them to zero to create a system of algebraic equations.

Step 6. Determine the values of $A_j\,(j=0,1,2,\cdots)$ and the remaining parameters by solving the system of algebraic equations with Maple or Mathematica, and insert these results into Eq. (3.4).

Step 7. The general form of the traveling wave solutions is obtained by returning to the original variables through Eq. (3.2).

Step 8. Equation (3.5) has four families of general solutions, depending on the parameters ρ,λ and σ:

Type 1. When $\rho^2-4\lambda\sigma>0$ and $\rho\lambda\neq 0$ or $\lambda\sigma\neq 0$, the solutions of Eq. (3.5) are:

$$G_1=-\frac{1}{2\lambda}\left(\rho+\sqrt{\Gamma_1}\tanh\left(\frac{\sqrt{\Gamma_1}}{2}\zeta\right)\right), \tag{3.6}$$

$$G_2=-\frac{1}{2\lambda}\left(\rho+\sqrt{\Gamma_1}\coth\left(\frac{\sqrt{\Gamma_1}}{2}\zeta\right)\right), \tag{3.7}$$

$$G_3=-\frac{1}{2\lambda}\left(\rho+\sqrt{\Gamma_1}\left(\tanh\left(\sqrt{\Gamma_1}\zeta\right)\pm i\,\mathrm{sech}\left(\sqrt{\Gamma_1}\zeta\right)\right)\right) \tag{3.8}$$

$$G_4=-\frac{1}{2\lambda}\left(\rho+\sqrt{\Gamma_1}\left(\coth\left(\sqrt{\Gamma_1}\zeta\right)\pm\mathrm{csch}\left(\sqrt{\Gamma_1}\zeta\right)\right)\right) \tag{3.9}$$

$$G_5=-\frac{1}{4\lambda}\left(2\rho+\sqrt{\Gamma_1}\left(\tanh\left(\frac{\sqrt{\Gamma_1}}{4}\zeta\right)+\coth\left(\frac{\sqrt{\Gamma_1}}{4}\zeta\right)\right)\right) \tag{3.10}$$

$$G_6=\frac{1}{2\lambda}\left(-\rho+\frac{\pm\sqrt{\Gamma_1\left(P^2+W^2\right)}-P\sqrt{\Gamma_1}\cosh\left(\sqrt{\Gamma_1}\zeta\right)}{P\sinh\left(\sqrt{\Gamma_1}\zeta\right)+W}\right), \tag{3.11}$$

$$G_7=\frac{1}{2\lambda}\left(-\rho-\frac{\pm\sqrt{\Gamma_1\left(P^2+W^2\right)}+P\sqrt{\Gamma_1}\cosh\left(\sqrt{\Gamma_1}\zeta\right)}{P\sinh\left(\sqrt{\Gamma_1}\zeta\right)+W}\right), \tag{3.12}$$

where P and W are two nonzero real constants.

$$G_8=\frac{2\sigma\cosh\left(\frac{\sqrt{\Gamma_1}}{2}\zeta\right)}{\sqrt{\Gamma_1}\sinh\left(\frac{\sqrt{\Gamma_1}}{2}\zeta\right)-\rho\cosh\left(\frac{\sqrt{\Gamma_1}}{2}\zeta\right)}, \tag{3.13}$$

$$G_9=\frac{-2\sigma\sinh\left(\frac{\sqrt{\Gamma_1}}{2}\zeta\right)}{\rho\sinh\left(\frac{\sqrt{\Gamma_1}}{2}\zeta\right)-\sqrt{\Gamma_1}\cosh\left(\frac{\sqrt{\Gamma_1}}{2}\zeta\right)}, \tag{3.14}$$

$$G_{10}=\frac{2\sigma\cosh\left(\sqrt{\Gamma_1}\zeta\right)}{\sqrt{\Gamma_1}\sinh\left(\sqrt{\Gamma_1}\zeta\right)-\rho\cosh\left(\sqrt{\Gamma_1}\zeta\right)\pm i\sqrt{\Gamma_1}}, \tag{3.15}$$

$$G_{11}=\frac{2\sigma\sinh\left(\sqrt{\Gamma_1}\zeta\right)}{-\rho\sinh\left(\sqrt{\Gamma_1}\zeta\right)+\sqrt{\Gamma_1}\cosh\left(\sqrt{\Gamma_1}\zeta\right)\pm\sqrt{\Gamma_1}}, \tag{3.16}$$

$$G_{12}=\frac{4\sigma\sinh\left(\frac{\sqrt{\Gamma_1}}{4}\zeta\right)\cosh\left(\frac{\sqrt{\Gamma_1}}{4}\zeta\right)}{-2\rho\sinh\left(\frac{\sqrt{\Gamma_1}}{4}\zeta\right)\cosh\left(\frac{\sqrt{\Gamma_1}}{4}\zeta\right)+\Gamma_3}, \tag{3.17}$$

where $\Gamma_1=\rho^2-4\lambda\sigma$ and $\Gamma_3=2\sqrt{\Gamma_1}\cosh^2\left(\frac{\sqrt{\Gamma_1}}{4}\zeta\right)-\sqrt{\Gamma_1}$.

Type 2. When $\rho^2-4\lambda\sigma<0$ and $\rho\lambda\neq 0$ or $\lambda\sigma\neq 0$, the solutions of Eq. (3.5) are:

$$G_{13}=\frac{1}{2\lambda}\left(-\rho+\sqrt{\Gamma_2}\tan\left(\frac{\sqrt{\Gamma_2}}{2}\zeta\right)\right), \tag{3.18}$$

$$G_{14}=-\frac{1}{2\lambda}\left(\rho+\sqrt{\Gamma_2}\cot\left(\frac{\sqrt{\Gamma_2}}{2}\zeta\right)\right), \tag{3.19}$$

$$G_{15}=\frac{1}{2\lambda}\left(-\rho+\sqrt{\Gamma_2}\left(\tan\left(\sqrt{\Gamma_2}\zeta\right)\pm\sec\left(\sqrt{\Gamma_2}\zeta\right)\right)\right) \tag{3.20}$$

$$G_{16}=-\frac{1}{2\lambda}\left(\rho+\sqrt{\Gamma_2}\left(\cot\left(\sqrt{\Gamma_2}\zeta\right)\pm\csc\left(\sqrt{\Gamma_2}\zeta\right)\right)\right) \tag{3.21}$$

$$G_{17}=\frac{1}{4\lambda}\left(-2\rho+\sqrt{\Gamma_2}\left(\tan\left(\frac{\sqrt{\Gamma_2}}{4}\zeta\right)-\cot\left(\frac{\sqrt{\Gamma_2}}{4}\zeta\right)\right)\right) \tag{3.22}$$

$$G_{18}=\frac{1}{2\lambda}\left(-\rho+\frac{\pm\sqrt{\Gamma_2\left(P^2-W^2\right)}-P\sqrt{\Gamma_2}\cos\left(\sqrt{\Gamma_2}\zeta\right)}{P\sin\left(\sqrt{\Gamma_2}\zeta\right)+W}\right), \tag{3.23}$$

$$G_{19}=\frac{1}{2\lambda}\left(-\rho-\frac{\pm\sqrt{\Gamma_2\left(P^2-W^2\right)}+P\sqrt{\Gamma_2}\cos\left(\sqrt{\Gamma_2}\zeta\right)}{P\sin\left(\sqrt{\Gamma_2}\zeta\right)+W}\right), \tag{3.24}$$

© 2027 NSP
Natural Sciences Publishing Cor.

where P and W are two nonzero real constants.

$$G_{20} = \frac{-2\sigma\cos\left(\frac{\sqrt{\Gamma_2}}{2}\zeta\right)}{\sqrt{\Gamma_2}\sin\left(\frac{\sqrt{\Gamma_2}}{2}\zeta\right)+\rho\cos\left(\frac{\sqrt{\Gamma_2}}{2}\zeta\right)}, \tag{3.25}$$

$$G_{21} = \frac{2\sigma\sin\left(\frac{\sqrt{\Gamma_2}}{2}\zeta\right)}{-\rho\sin\left(\frac{\sqrt{\Gamma_2}}{2}\zeta\right)+\sqrt{\Gamma_2}\cos\left(\frac{\sqrt{\Gamma_2}}{2}\zeta\right)}, \tag{3.26}$$

$$G_{22} = \frac{-2\sigma\cos\left(\sqrt{\Gamma_2}\zeta\right)}{\sqrt{\Gamma_2}\sin\left(\sqrt{\Gamma_2}\zeta\right)+\rho\cos\left(\sqrt{\Gamma_2}\zeta\right)\pm\sqrt{\Gamma_2}}, \tag{3.27}$$

$$G_{23} = \frac{2\sigma\sin\left(\sqrt{\Gamma_2}\zeta\right)}{-\rho\sin\left(\sqrt{\Gamma_2}\zeta\right)+\sqrt{\Gamma_2}\cos\left(\sqrt{\Gamma_2}\zeta\right)\pm\sqrt{\Gamma_2}}, \tag{3.28}$$

$$G_{24} = \frac{4\sigma\sin\left(\frac{\sqrt{\Gamma_2}}{4}\zeta\right)\cos\left(\frac{\sqrt{\Gamma_2}}{4}\zeta\right)}{-2\rho\sin\left(\frac{\sqrt{\Gamma_2}}{4}\zeta\right)\cos\left(\frac{\sqrt{\Gamma_2}}{4}\zeta\right)+\Gamma_4}, \tag{3.29}$$

where $\Gamma_2 = 4\lambda\sigma-\rho^2$ and $\Gamma_4 = 2\sqrt{\Gamma_2}\cos^2\left(\frac{\sqrt{\Gamma_2}}{4}\zeta\right)-\sqrt{\Gamma_2}$.

Type 3. When $\sigma = 0$ and $\rho\lambda \neq 0$, the solutions of Eq. (3.5) become:

$$G_{25} = \frac{-\rho f_1}{\lambda\left(f_1+\cosh(\rho\zeta)-\sinh(\rho\zeta)\right)}, \tag{3.30}$$

$$G_{26} = \frac{-\rho\left(\cosh(\rho\zeta)+\sinh(\rho\zeta)\right)}{\lambda\left(f_1+\cosh(\rho\zeta)+\sinh(\rho\zeta)\right)}, \tag{3.31}$$

where f_1 is an arbitrary constant.

Type 4. When $\lambda \neq 0$ and $\sigma = \rho = 0$, the solution of Eq. (3.5) becomes:

$$G_{27} = \frac{-1}{\lambda\zeta+l_1}, \tag{3.32}$$

where l_1 is an arbitrary constant.

4 Application of the extended generalized Riccati equation mapping method

Since Q'' and Q^3 must be in homogeneous balance in Eq. (2.5), we find that $n = 1$. Thus, $Q(\zeta)$ has the form

$$Q(\zeta) = A_0 + A_1\left(\frac{G'}{G}\right), \tag{4.1}$$

and, using Eq. (3.5),

$$Q(\zeta) = A_0 + \frac{A_1\left(\sigma+\rho G+\lambda G^2\right)}{G}, \tag{4.2}$$

where A_0 and A_1 are constants to be determined. These constants are obtained by substituting Eq. (4.2) into Eq. (2.5), collecting all terms with the same power of G^i, and setting all coefficients to zero. This produces the following system of algebraic equations:

$$\begin{cases}
-2k^2\gamma_0{}^2\delta_1{}^4A_1\lambda^3+12h^2\beta A_1{}^3\lambda^3\\
-2k^2\rho_0{}^2\delta_2{}^4A_1\lambda^3=0,\\
-3k^2\gamma_0{}^2\delta_1{}^4A_1\rho\lambda^2-3k^2\rho_0{}^2\delta_2{}^4A_1\rho\lambda^2\\
-12h^2\alpha A_1{}^2\lambda^2+36h^2\beta A_1{}^3\rho\lambda^2\\
+36h^2\beta A_0A_1{}^2\lambda^2=0,\\
36h^2\beta A_1{}^3\rho^2\lambda+72h^2\beta A_0A_1{}^2\rho\lambda\\
-k^2\rho_0{}^2\delta_2{}^4A_1\rho^2\lambda+36h^2\beta A_0{}^2A_1\lambda\\
-24h^2\alpha A_1{}^2\rho\lambda-k^2\gamma_0{}^2\delta_1{}^4A_1\rho^2\lambda\\
+12h^2A_1\lambda-2k^2\rho_0{}^2\delta_2{}^4A_1\lambda^2\sigma\\
-12\gamma_0{}^2\delta_1{}^2A_1\lambda+36h^2\beta A_1{}^3\sigma\lambda^2\\
-24h^2\alpha A_0A_1\lambda-2k^2\gamma_0{}^2\delta_1{}^4A_1\lambda^2\sigma\\
-12\rho_0{}^2\delta_2{}^2A_1\lambda=0,\\
-2k^2\gamma_0{}^2\delta_1{}^4A_1\rho\lambda\sigma\\
-2k^2\rho_0{}^2\delta_2{}^4A_1\rho\lambda\sigma+36h^2\beta A_0{}^2A_1\rho\\
-12\rho_0{}^2\delta_2{}^2A_1\rho-24h^2\alpha A_0A_1\rho\\
+12h^2A_0+12h^2A_1\rho-12\gamma_0{}^2\delta_1{}^2A_1\rho\\
+12h^2\beta A_1{}^3\rho^3+72h^2\beta A_1{}^3\sigma\rho\lambda\\
-24h^2\alpha A_1{}^2\sigma\lambda+12h^2\beta A_0{}^3\\
-12h^2\alpha A_1{}^2\rho^2+36h^2\beta A_0A_1{}^2\rho^2\\
-12\gamma_0{}^2\delta_1{}^2A_0-12\rho_0{}^2\delta_2{}^2A_0\\
+72h^2\beta A_0A_1{}^2\sigma\lambda-12h^2\alpha A_0{}^2=0,\\
-12\gamma_0{}^2\delta_1{}^2A_1\sigma-24h^2\alpha A_0A_1\sigma\\
-24h^2\alpha A_1{}^2\sigma\rho+12h^2A_1\sigma\\
+36h^2\beta A_1{}^3\sigma^2\lambda-k^2\gamma_0{}^2\delta_1{}^4A_1\rho^2\sigma\\
+36h^2\beta A_0{}^2A_1\sigma-2k^2\gamma_0{}^2\delta_1{}^4A_1\sigma^2\lambda\\
+36h^2\beta A_1{}^3\sigma\rho^2-12\rho_0{}^2\delta_2{}^2A_1\sigma\\
-k^2\rho_0{}^2\delta_2{}^4A_1\rho^2\sigma-2k^2\rho_0{}^2\delta_2{}^4A_1\sigma^2\lambda\\
+72h^2\beta A_0A_1{}^2\sigma\rho=0,\\
-3k^2\gamma_0{}^2\delta_1{}^4A_1\sigma^2\rho+36h^2\beta A_1{}^3\sigma^2\rho\\
-3k^2\rho_0{}^2\delta_2{}^4A_1\sigma^2\rho-12h^2\alpha A_1{}^2\sigma^2\\
+36h^2\beta A_0A_1{}^2\sigma^2=0,\\
12h^2\beta A_1{}^3\sigma^3-2k^2\rho_0{}^2\delta_2{}^4A_1\sigma^3\\
-2k^2\gamma_0{}^2\delta_1{}^4A_1\sigma^3=0.
\end{cases} \tag{4.3}$$

With the use of Maple, we solve the system of algebraic equations Eq. (4.3), which yields

$$\begin{cases}
A_0 = \frac{1}{12}\,\frac{2\sqrt{6}\left(\beta\,(SS)\right)^{3/2}k\rho-4\beta\left(\frac{1}{4}\rho\sqrt{\beta\,(SS)}\sqrt{6}k+\alpha h\right)(SS)}{h\beta^2\,(SS)},\\
A_1 = \frac{1}{6}\,\frac{\sqrt{6}\sqrt{\beta\,(SS)}k}{\beta h},\\
h \text{ arbitrary}.
\end{cases} \tag{4.4}$$

By inserting Eq. (4.4) and Eq. (4.2) into Eq. (2.2), we obtain the following exact solutions of Eq. (2.1).

Type 1. The traveling wave solutions of Eq. (3.5) when

© 2027 NSP
Natural Sciences Publishing Cor.

$\rho^2-4\lambda\sigma>0$ and $\rho\lambda\neq 0$ or $\lambda\sigma\neq 0$, are:

$$U_1(x,y,t)=\mp\frac{1}{12}\frac{2\sqrt{6}\left(\beta\,(SS)\right)^{3/2}k\rho-4\beta\left(\frac{1}{4}\rho\sqrt{\beta\,(SS)}\sqrt{6}k+\alpha h\right)(SS)}{h\beta^2\,(SS)}\pm\frac{1}{6}\frac{\sqrt{6}\sqrt{\beta\,(SS)}k}{\beta h}\left(\frac{2\Phi_1^2\,\mathrm{sech}^2(\Phi_1\zeta)}{\rho+2\Phi_1\tanh(\Phi_1\zeta)}\right),\quad(4.5)$$

$$U_2(x,y,t)=\mp\frac{1}{12}\frac{2\sqrt{6}\left(\beta\,(SS)\right)^{3/2}k\rho-4\beta\left(\frac{1}{4}\rho\sqrt{\beta\,(SS)}\sqrt{6}k+\alpha h\right)(SS)}{h\beta^2\,(SS)}\pm\frac{1}{6}\frac{\sqrt{6}\sqrt{\beta\,(SS)}k}{\beta h}\left(\frac{2\Phi_1^2\,\mathrm{csch}^2(\Phi_1\zeta)}{\rho+2\Phi_1\coth(\Phi_1\zeta)}\right),\quad(4.6)$$

$$U_3(x,y,t)=\mp\frac{1}{12}\frac{2\sqrt{6}\left(\beta\,(SS)\right)^{3/2}k\rho-4\beta\left(\frac{1}{4}\rho\sqrt{\beta\,(SS)}\sqrt{6}k+\alpha h\right)(SS)}{h\beta^2\,(SS)}\pm\frac{1}{6}\frac{\sqrt{6}\sqrt{\beta\,(SS)}k}{\beta h}\left(\frac{4\Phi_1^2\,\mathrm{sech}(2\,\Phi_1\zeta)(1\mp i\sinh(2\Phi_1\zeta))}{\rho\cosh(2\Phi_1\zeta)+2\Phi_1\sinh(2\,\Phi_1\zeta)\pm 2i\Phi_1}\right),\quad(4.7)$$

$$U_4(x,y,t)=\mp\frac{1}{12}\frac{2\sqrt{6}\left(\beta\,(SS)\right)^{3/2}k\rho-4\beta\left(\frac{1}{4}\rho\sqrt{\beta\,(SS)}\sqrt{6}k+\alpha h\right)(SS)}{h\beta^2\,(SS)}\pm\frac{1}{6}\frac{\sqrt{6}\sqrt{\beta\,(SS)}k}{\beta h}\left(\frac{2\Phi_1^2\,\mathrm{csch}(\Phi_1\zeta)}{\rho\sinh(\Phi_1\zeta)+2\Phi_1\cosh(\Phi_1\zeta)}\right),\quad(4.8)$$

$$U_5(x,y,t)=\mp\frac{1}{12}\frac{2\sqrt{6}\left(\beta\,(SS)\right)^{3/2}k\rho-4\beta\left(\frac{1}{4}\rho\sqrt{\beta\,(SS)}\sqrt{6}k+\alpha h\right)(SS)}{h\beta^2\,(SS)}\pm\frac{1}{6}\frac{\sqrt{6}\sqrt{\beta\,(SS)}k}{\beta h}\left(\frac{4\Phi_1^2\,\mathrm{csch}(2\,\Phi_1\zeta)}{\rho\tanh(\Phi_1\zeta)+2\Phi_1}\right),\quad(4.9)$$

$$U_6(x,y,t)=\mp\frac{1}{12}\frac{2\sqrt{6}\left(\beta\,(SS)\right)^{3/2}k\rho-4\beta\left(\frac{1}{4}\rho\sqrt{\beta\,(SS)}\sqrt{6}k+\alpha h\right)(SS)}{h\beta^2\,(SS)}\pm\frac{1}{6}\frac{\sqrt{6}\sqrt{\beta\,(SS)}k}{\beta h}\left(\frac{4P\Phi_1^2\left(P-W\sinh(2\,\Phi_1\zeta)-\sqrt{P^2+W^2}\cosh(2\Phi_1\zeta)\right)}{(P\sinh(2\,\Phi_1\zeta)+W)\Omega_1}\right),\quad(4.10)$$

$$U_7(x,y,t)=\mp\frac{1}{12}\frac{2\sqrt{6}\left(\beta\,(SS)\right)^{3/2}k\rho-4\beta\left(\frac{1}{4}\rho\sqrt{\beta\,(SS)}\sqrt{6}k+\alpha h\right)(SS)}{h\beta^2\,(SS)}\pm\frac{1}{6}\frac{\sqrt{6}\sqrt{\beta\,(SS)}k}{\beta h}\left(\frac{4P\Phi_1^2\left(P-W\sinh(2\,\Phi_1\zeta)+\sqrt{P^2+W^2}\cosh(2\Phi_1\zeta)\right)}{(P\sinh(2\,\Phi_1\zeta)+W)\Omega_2}\right),\quad(4.11)$$

where

$$\Omega_1=\rho P\sinh(2\Phi_1\zeta)+\rho W-2\Phi_1\sqrt{P^2+W^2}+2P\Phi_1\cosh(2\Phi_1\zeta),$$

$$\Omega_2=\rho P\sinh(2\Phi_1\zeta)+\rho W+2\Phi_1\sqrt{P^2+W^2}+2P\Phi_1\cosh(2\Phi_1\zeta),$$

and P and W are two nonzero real constants.

$$U_8(x,y,t)=\mp\frac{1}{12}\frac{2\sqrt{6}\left(\beta\,(SS)\right)^{3/2}k\rho-4\beta\left(\frac{1}{4}\rho\sqrt{\beta\,(SS)}\sqrt{6}k+\alpha h\right)(SS)}{h\beta^2\,(SS)}\pm\frac{1}{6}\frac{\sqrt{6}\sqrt{\beta\,(SS)}k}{\beta h}\left(\frac{2\Phi_1^2\,\mathrm{sech}(\Phi_1\zeta)}{2\Phi_1\sinh(\Phi_1\zeta)-\rho\cosh(\Phi_1\zeta)}\right),\quad(4.12)$$

$$U_9(x,y,t)=\mp\frac{1}{12}\frac{2\sqrt{6}\left(\beta\,(SS)\right)^{3/2}k\rho-4\beta\left(\frac{1}{4}\rho\sqrt{\beta\,(SS)}\sqrt{6}k+\alpha h\right)(SS)}{h\beta^2\,(SS)}\pm\frac{1}{6}\frac{\sqrt{6}\sqrt{\beta\,(SS)}k}{\beta h}\left(\frac{2\Phi_1^2\,\mathrm{csch}(\Phi_1\zeta)}{2\Phi_1\cosh(\Phi_1\zeta)-\rho\sinh(\Phi_1\zeta)}\right),\quad(4.13)$$

$$U_{10}(x,y,t)=\mp\frac{1}{12}\frac{2\sqrt{6}\left(\beta\,(SS)\right)^{3/2}k\rho-4\beta\left(\frac{1}{4}\rho\sqrt{\beta\,(SS)}\sqrt{6}k+\alpha h\right)(SS)}{h\beta^2\,(SS)}\pm\frac{1}{6}\frac{\sqrt{6}\sqrt{\beta\,(SS)}k}{\beta h}\left(\frac{4\Phi_1^2\,\mathrm{sech}(2\,\Phi_1\zeta)(1\mp i\sinh(2\Phi_1\zeta))}{\rho\cosh(2\Phi_1\zeta)-2\Phi_1\sinh(2\,\Phi_1\zeta)\mp 2i\Phi_1}\right),\quad(4.14)$$

$$U_{11}(x,y,t)=\mp\frac{1}{12}\frac{2\sqrt{6}\left(\beta\,(SS)\right)^{3/2}k\rho-4\beta\left(\frac{1}{4}\rho\sqrt{\beta\,(SS)}\sqrt{6}k+\alpha h\right)(SS)}{h\beta^2\,(SS)}\pm\frac{1}{6}\frac{\sqrt{6}\sqrt{\beta\,(SS)}k}{\beta h}\left(\frac{4\Phi_1^2\,\mathrm{csch}(2\,\Phi_1\zeta)(1\pm\cosh(2\Phi_1\zeta))}{2\Phi_1\cosh(2\Phi_1\zeta)-\rho\sinh(2\Phi_1\zeta)\pm 2\Phi_1}\right),\quad(4.15)$$

$$U_{12}(x,y,t)=\mp\frac{1}{12}\frac{2\sqrt{6}\left(\beta\,(SS)\right)^{3/2}k\rho-4\beta\left(\frac{1}{4}\rho\sqrt{\beta\,(SS)}\sqrt{6}k+\alpha h\right)(SS)}{h\beta^2\,(SS)}\pm\frac{1}{6}\frac{\sqrt{6}\sqrt{\beta\,(SS)}k}{\beta h}\left(\frac{2\Phi_1^2\,\mathrm{csch}(\Phi_1\zeta)}{2\Phi_1\cosh(\Phi_1\zeta)-\rho\sinh(\Phi_1\zeta)}\right),\quad(4.16)$$

where $\Phi_1=\frac{1}{2}\sqrt{\rho^2-4\lambda\sigma}$ and $\zeta=k(x+y-ht)$.

Type 2. The traveling wave solutions of Eq. (3.5) when

© 2027 NSP
Natural Sciences Publishing Cor.

$\rho^2-4\lambda\sigma<0$ and $\rho\lambda\neq 0$ or $\lambda\sigma\neq 0$ are:

$$U_{13}(x,y,t)=\mp\frac{1}{12}\frac{2\sqrt{6}(\beta(SS))^{3/2}k\rho-4\beta\left(\frac{1}{4}\rho\sqrt{\beta(SS)}\sqrt{6}k+\alpha h\right)(SS)}{h\beta^2(SS)}\pm\frac{1}{6}\frac{\sqrt{6}\sqrt{\beta(SS)}k}{\beta h}\left(\frac{2\Phi_2^2\sec^2(\Phi_2\zeta)}{-\rho+2\Phi_2\tan(\Phi_2\zeta)}\right),\quad(4.17)$$

$$U_{14}(x,y,t)=\mp\frac{1}{12}\frac{2\sqrt{6}(\beta(SS))^{3/2}k\rho-4\beta\left(\frac{1}{4}\rho\sqrt{\beta(SS)}\sqrt{6}k+\alpha h\right)(SS)}{h\beta^2(SS)}\pm\frac{1}{6}\frac{\sqrt{6}\sqrt{\beta(SS)}k}{\beta h}\left(\frac{2\Phi_2^2\csc^2(\Phi_2\zeta)}{\rho+2\Phi_2\cot(\Phi_2\zeta)}\right),\quad(4.18)$$

$$U_{15}(x,y,t)=\mp\frac{1}{12}\frac{2\sqrt{6}(\beta(SS))^{3/2}k\rho-4\beta\left(\frac{1}{4}\rho\sqrt{\beta(SS)}\sqrt{6}k+\alpha h\right)(SS)}{h\beta^2(SS)}\pm\frac{1}{6}\frac{\sqrt{6}\sqrt{\beta(SS)}k}{\beta h}\left(\frac{4\Phi_2^2\sec(2\Phi_2\zeta)(1\pm\sin(2\Phi_2\zeta))}{-\rho\cos(2\Phi_2\zeta)+2\Phi_2\sin(2\Phi_2\zeta)\pm 2\Phi_2}\right),\quad(4.19)$$

$$U_{16}(x,y,t)=\mp\frac{1}{12}\frac{2\sqrt{6}(\beta(SS))^{3/2}k\rho-4\beta\left(\frac{1}{4}\rho\sqrt{\beta(SS)}\sqrt{6}k+\alpha h\right)(SS)}{h\beta^2(SS)}\pm\frac{1}{6}\frac{\sqrt{6}\sqrt{\beta(SS)}k}{\beta h}\left(\frac{2\Phi_2^2\sec(\Phi_2\zeta)}{\rho\cos(\Phi_2\zeta)+2\Phi_2\sin(\Phi_2\zeta)}\right),\quad(4.20)$$

$$U_{17}(x,y,t)=\mp\frac{1}{12}\frac{2\sqrt{6}(\beta(SS))^{3/2}k\rho-4\beta\left(\frac{1}{4}\rho\sqrt{\beta(SS)}\sqrt{6}k+\alpha h\right)(SS)}{h\beta^2(SS)}\pm\frac{1}{6}\frac{\sqrt{6}\sqrt{\beta(SS)}k}{\beta h}\left(\frac{2\Phi_2^2\csc(\Phi_2\zeta)}{\rho\sin(\Phi_2\zeta)+2\Phi_2\cos(\Phi_2\zeta)}\right),\quad(4.21)$$

$$U_{18}(x,y,t)=\mp\frac{1}{12}\frac{2\sqrt{6}(\beta(SS))^{3/2}k\rho-4\beta\left(\frac{1}{4}\rho\sqrt{\beta(SS)}\sqrt{6}k+\alpha h\right)(SS)}{h\beta^2(SS)}\pm\frac{1}{6}\frac{\sqrt{6}\sqrt{\beta(SS)}k}{\beta h}\left(\frac{4P\Phi_2^2\left(\sqrt{P^2-W^2}\cos(2\Phi_2\zeta)-W\sin(2\Phi_2\zeta)-P\right)}{(P\sin(2\Phi_2\zeta)+W)\Omega_3}\right),\quad(4.22)$$

$$U_{19}(x,y,t)=\mp\frac{1}{12}\frac{2\sqrt{6}(\beta(SS))^{3/2}k\rho-4\beta\left(\frac{1}{4}\rho\sqrt{\beta(SS)}\sqrt{6}k+\alpha h\right)(SS)}{h\beta^2(SS)}\pm\frac{1}{6}\frac{\sqrt{6}\sqrt{\beta(SS)}k}{\beta h}\left(\frac{4P\Phi_2^2\left(\sqrt{P^2-W^2}\cos(2\Phi_2\zeta)+W\sin(2\Phi_2\zeta)+P\right)}{(P\sin(2\Phi_2\zeta)+W)\Omega_4}\right),\quad(4.23)$$

where

$$\begin{aligned}\Omega_3&=\rho P\sin(2\Phi_2\zeta)+2P\Phi_2\cos(2\Phi_2\zeta)\\&\quad+\rho W-2\Phi_2\sqrt{P^2-W^2},\\\Omega_4&=\rho P\sin(2\Phi_2\zeta)+2P\Phi_2\cos(2\Phi_2\zeta)\\&\quad+\rho W+2\Phi_2\sqrt{P^2-W^2},\end{aligned}\quad(4.24)$$

and P and W are two nonzero real constants.

$$U_{20}(x,y,t)=\mp\frac{1}{12}\frac{2\sqrt{6}(\beta(SS))^{3/2}k\rho-4\beta\left(\frac{1}{4}\rho\sqrt{\beta(SS)}\sqrt{6}k+\alpha h\right)(SS)}{h\beta^2(SS)}\pm\frac{1}{6}\frac{\sqrt{6}\sqrt{\beta(SS)}k}{\beta h}\left(\frac{4\Phi_2^2\csc(2\Phi_2\zeta)}{\rho\cot(\Phi_2\zeta)+2\Phi_2}\right),\quad(4.25)$$

$$U_{21}(x,y,t)=\mp\frac{1}{12}\frac{2\sqrt{6}(\beta(SS))^{3/2}k\rho-4\beta\left(\frac{1}{4}\rho\sqrt{\beta(SS)}\sqrt{6}k+\alpha h\right)(SS)}{h\beta^2(SS)}\pm\frac{1}{6}\frac{\sqrt{6}\sqrt{\beta(SS)}k}{\beta h}\left(\frac{4\Phi_2^2\csc(2\Phi_2\zeta)}{\rho\tan(\Phi_2\zeta)+2\Phi_2}\right),\quad(4.26)$$

$$U_{22}(x,y,t)=\mp\frac{1}{12}\frac{2\sqrt{6}(\beta(SS))^{3/2}k\rho-4\beta\left(\frac{1}{4}\rho\sqrt{\beta(SS)}\sqrt{6}k+\alpha h\right)(SS)}{h\beta^2(SS)}\pm\frac{1}{6}\frac{\sqrt{6}\sqrt{\beta(SS)}k}{\beta h}\left(\frac{2\Phi_2^2\sec(2\Phi_2\zeta)(1\pm\sin(2\Phi_2\zeta))(\rho\cos(2\Phi_2\zeta)+2\Phi_2\sin(2\Phi_2\zeta)\pm 2\Phi_2)}{(\rho^2-2\lambda\sigma)\cos^2(2\Phi_2\zeta)+2\Phi_2(1\pm\sin(2\Phi_2\zeta))(2\Phi_2\pm\rho\cos(2\Phi_2\zeta))}\right),\quad(4.27)$$

$$U_{23}(x,y,t)=\mp\frac{1}{12}\frac{2\sqrt{6}(\beta(SS))^{3/2}k\rho-4\beta\left(\frac{1}{4}\rho\sqrt{\beta(SS)}\sqrt{6}k+\alpha h\right)(SS)}{h\beta^2(SS)}\pm\frac{1}{6}\frac{\sqrt{6}\sqrt{\beta(SS)}k}{\beta h}\left(\frac{4\Phi_2^2\csc(2\Phi_2\zeta)(1\pm\cos(2\Phi_2\zeta))}{-\rho\sin(2\Phi_2\zeta)+2\Phi_2\cos(2\Phi_2\zeta)\pm 2\Phi_2}\right),\quad(4.28)$$

$$U_{24}(x,y,t)=\mp\frac{1}{12}\frac{2\sqrt{6}(\beta(SS))^{3/2}k\rho-4\beta\left(\frac{1}{4}\rho\sqrt{\beta(SS)}\sqrt{6}k+\alpha h\right)(SS)}{h\beta^2(SS)}\pm\frac{1}{6}\frac{\sqrt{6}\sqrt{\beta(SS)}k}{\beta h}\left(\frac{2\Phi_2^2\csc(\Phi_2\zeta)}{\rho\sin(\Phi_2\zeta)+2\Phi_2\cos(\Phi_2\zeta)}\right),\quad(4.29)$$

where $\Phi_2=\frac{1}{2}\sqrt{4\lambda\sigma-\rho^2}$ and $\zeta=k(x+y-ht)$.

Type 3. The traveling wave solutions of Eq. (3.5) when

© 2027 NSP
Natural Sciences Publishing Cor.

$\sigma = 0$ and $\rho\lambda \neq 0$ are:

$$U_{25}(x,y,t) = \mp\frac{1}{12}\frac{2\sqrt{6}(\beta(SS))^{3/2}k\rho - 4\beta\left(\frac{1}{4}\rho\sqrt{\beta(SS)}\sqrt{6}k+\alpha h\right)(SS)}{h\beta^2(SS)} \pm\frac{1}{6}\frac{\sqrt{6}\sqrt{\beta(SS)}k}{\beta h}\left(\frac{\rho(\cosh(\rho\zeta)-\sinh(\rho\zeta))}{f_1+\cosh(\rho\zeta)-\sinh(\rho\zeta)}\right), \quad (4.30)$$

$$U_{26}(x,y,t) = \mp\frac{1}{12}\frac{2\sqrt{6}(\beta(SS))^{3/2}k\rho - 4\beta\left(\frac{1}{4}\rho\sqrt{\beta(SS)}\sqrt{6}k+\alpha h\right)(SS)}{h\beta^2(SS)} \pm\frac{1}{6}\frac{\sqrt{6}\sqrt{\beta(SS)}k}{\beta h}\left(\frac{\rho f_1}{f_1+\cosh(\rho\zeta)+\sinh(\rho\zeta)}\right), \quad (4.31)$$

where f_1 is an arbitrary constant and $\zeta = k(x+y-ht)$.

Type 4. When $\lambda \neq 0$ and $\sigma = \rho = 0$, the traveling wave solution of Eq. (3.5) becomes:

$$U_{27}(x,y,t) = \mp\frac{1}{12}\frac{2\sqrt{6}(\beta(SS))^{3/2}k\rho - 4\beta\left(\frac{1}{4}\rho\sqrt{\beta(SS)}\sqrt{6}k+\alpha h\right)(SS)}{h\beta^2(SS)} \pm\frac{1}{6}\frac{\sqrt{6}\sqrt{\beta(SS)}k}{\beta h}\left(\frac{\lambda}{\lambda\zeta+l_1}\right), \quad (4.32)$$

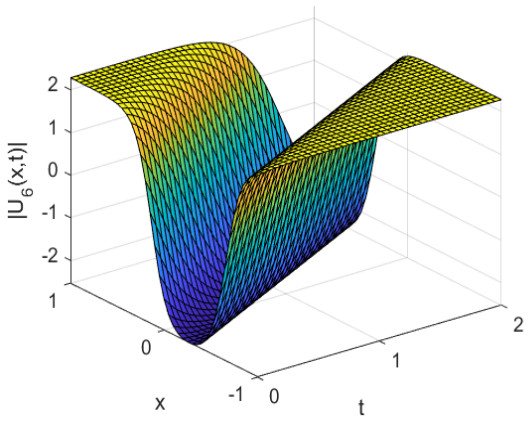
where l_1 is an arbitrary constant and $\zeta = k(x+y-ht)$.

5 The graphical representation

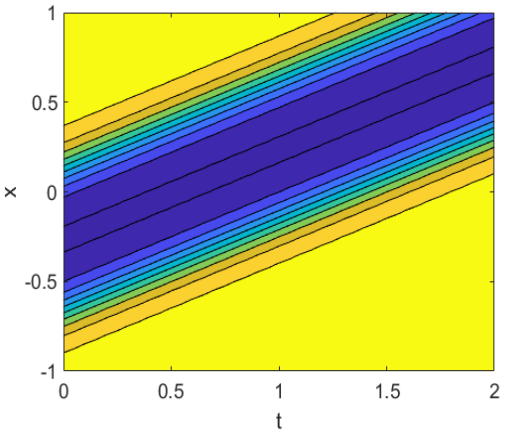
This section presents the nonlinear telecommunication model solutions in 3-D and contour form.

The graphical representations provide a comprehensive illustration of the different wave structures generated by the nonlinear telecommunication model. The three-dimensional plots in Figures 1(a)–16(a) demonstrate the amplitude, shape, and spatial distribution of the obtained wave solutions, whereas the corresponding contour plots in Figures 1(b)–16(b) provide additional insight into their propagation patterns and spatial localization. The figures reveal several distinct nonlinear wave behaviours, including bright solitons, dark solitons, singular solitons, periodic waves, and rational solutions. These different structures arise from the various families of solutions of the generalized Riccati equation and demonstrate the considerable flexibility of the proposed analytical method.

Figure **??** displays a combo of bright-dark soliton wave solution when $h = 0.5, k = 1, \rho = 12, \lambda = 0.5, \sigma = 0.5, P = 1, W = 1.2, \alpha = 0.5, \beta = 0.5, \gamma_0 = 0.5, \rho_0 = 0.5, \delta_1 = 5, \delta_2 = 5$. Figure 1 illustrates a combination of bright and dark soliton structures. The three-dimensional surface displays a pronounced localized transition between regions of relatively high and low amplitudes, producing a characteristic wave profile. The contour representation further reveals a well-defined propagation pattern, with closely spaced parallel contours surrounding the principal wave structure. This combination indicates the coexistence of different wave characteristics within a single analytical solution. The localized transition between the upper and lower amplitude regions demonstrates how nonlinear effects contribute to the formation of distinct wave profiles in the telecommunication model. Such structures are particularly relevant to understanding the propagation and modulation of optical signals in nonlinear transmission media.



(a)



(b)

Fig. 1: 3-D (a) and contour (b) visualization of $|U_6(x,y,t)|$.

Figure **??** displays a combo of singular-bright soliton wave solution when $h = 0.5, k = 1,$

© 2027 NSP
Natural Sciences Publishing Cor.

$\rho = 12, \lambda = 0.1, \sigma = 0.1, P = 0.5, W = 1.2, \alpha = 0.5, \beta = 1, \gamma_0 = 0.5, \rho_0 = 0.05, \delta_1 = 1, \delta_2 = 0.1$. Figure 2 presents a combination of singular and bright soliton wave structures. The three-dimensional representation exhibits a pronounced elevated wave profile accompanied by a singular feature, indicating the presence of a localized region with significantly enhanced amplitude. The corresponding contour plot shows a concentrated band of high amplitude surrounded by regions of lower intensity. Compared with Figure 1, the wave profile exhibits a more pronounced amplitude variation, suggesting that changes in the governing parameters can significantly influence the geometry and intensity of the resulting solution. The coexistence of bright and singular characteristics demonstrates the ability of the model to generate more complex nonlinear wave configurations.

Figure 1 displays a singular soliton wave solution when $h = 0.5, k = 1, \rho = 12, \lambda = 0.1, \sigma = 0.1, P = 0.5, W = 1.2, \alpha = 0.5, \beta = 1, \gamma_0 = 0.5, \rho_0 = 0.05, \delta_1 = 1, \delta_2 = 0.1$. Figure 3 depicts a singular soliton solution characterized by a distinct variation in amplitude across the spatial domain. The three-dimensional surface reveals a pronounced depression and an adjacent elevated region, producing a characteristic singular wave profile. The contour plot displays several parallel bands that distinguish the regions of different amplitude. The concentration of these contours around the transition region indicates a relatively sharp spatial variation in the wave profile. This behaviour illustrates the influence of nonlinear interactions on the formation of localized wave structures and demonstrates the importance of the model parameters in determining the amplitude distribution and geometrical characteristics of the solution.

Figure **??** displays a singular soliton wave solution when $h = 0.005, k = 1, \rho = 12, \lambda = 0.1, \sigma = 0.1, P = 0.5, W = 1.2, \alpha = 0.5, \beta = 1, \gamma_0 = 0.5, \rho_0 = 0.005, \delta_1 = 1, \delta_2 = 0.1$. Figure 4 also represents a singular soliton solution; however, its graphical structure differs considerably from that of Figure 3. The three-dimensional surface exhibits several sharply separated regions with large amplitude variations, including pronounced vertical transitions. These features are associated with the singular behaviour of the analytical solution, where the wave amplitude becomes strongly enhanced near particular spatial locations. The contour representation displays distinct horizontal bands separated by narrow transition regions. This indicates that the wave structure maintains clearly differentiated amplitude regions throughout the considered time interval. The comparison between Figures 3 and 4 highlights the sensitivity of singular wave configurations to variations in the governing parameters, particularly those associated with the propagation characteristics and transverse spatial effects.

Figure 2 displays a combo of bright-singular soliton wave solution when $h = 0.05, k = 1, \rho = 12, \lambda = 0.1, \sigma = 0.1, P = 0.5, W = 1.2, \alpha = 0.5, \beta = 1, \gamma_0 = 0.5, \rho_0 = 0.005, \delta_1 = 1, \delta_2 = 0.1$. Figure 5 illustrates a combination of bright and singular soliton structures. The three-dimensional surface presents a pronounced transition between regions of negative and positive amplitudes, together with a localized elevated region. This configuration reflects the coexistence of a bright wave component and singular characteristics within the same solution. The contour plot exhibits relatively narrow and well-defined bands, indicating the presence of distinct amplitude regions separated by sharp spatial transitions. The graphical behaviour demonstrates that the nonlinear telecommunication equation admits wave structures with more complicated geometries than conventional bright or dark solitons. Such solutions provide additional analytical possibilities for describing nonlinear signal propagation in communication systems.

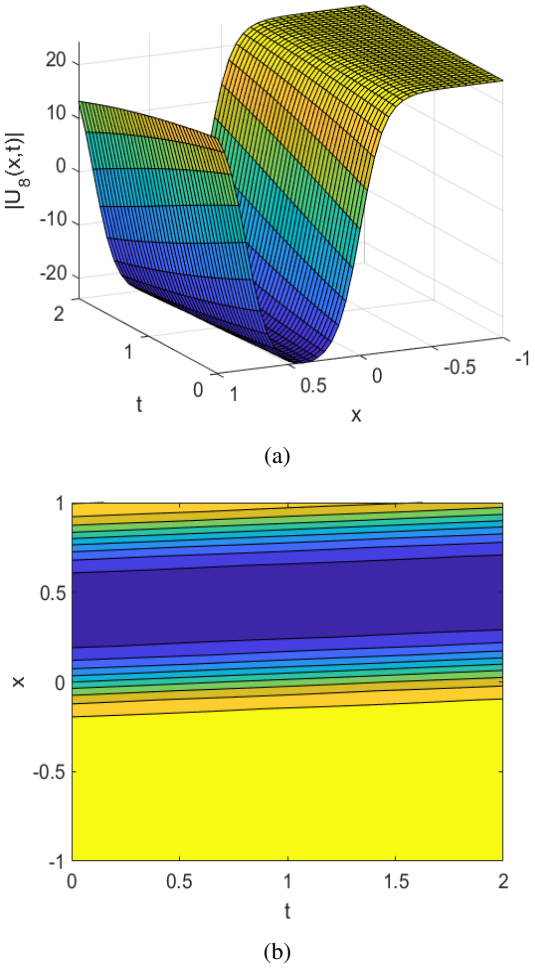
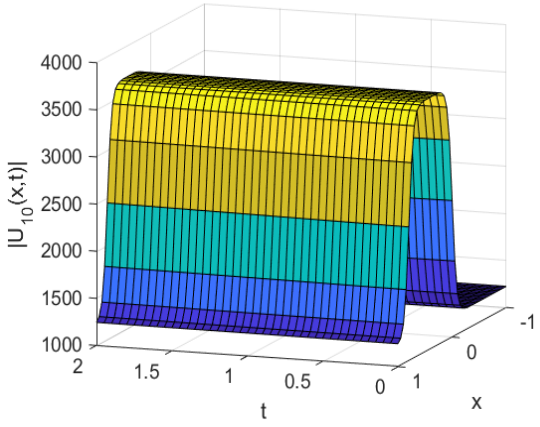
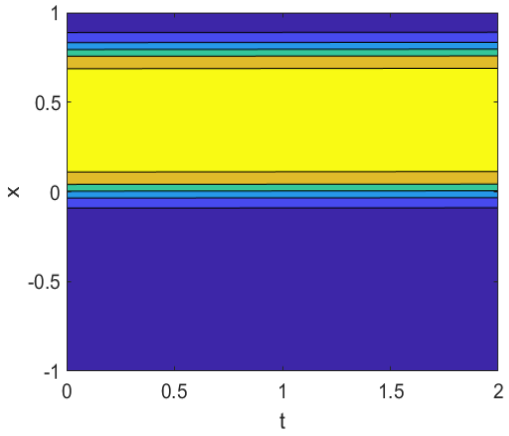


Fig. 2: 3-D (a) and contour (b) visualization of $|U_8(x,y,t)|$.

© 2027 NSP
Natural Sciences Publishing Cor.



(a)

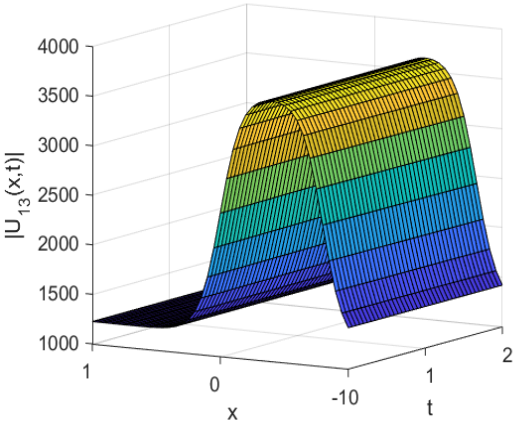


(b)

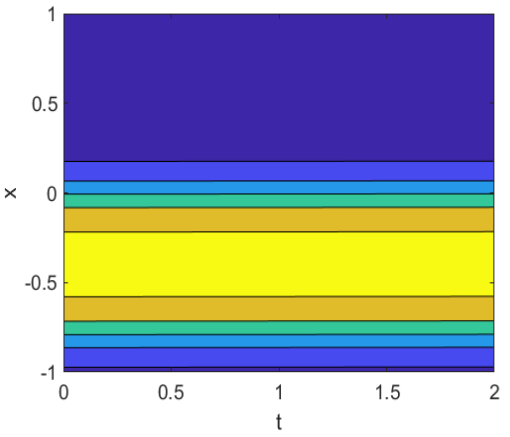
Fig. 3: 3-D (a) and contour (b) visualization of $|U_{10}(x,y,t)|$.

Figure 3 displays a combo of bright-singular soliton wave solution when $h = 0.001, k = 1, \rho = 12, \lambda = 0.1, \sigma = 0.1, P = 0.5, W = 1.2, \alpha = 0.5, \beta = 1, \gamma_0 = 0.5, \rho_0 = 0.005, \delta_1 = 1, \delta_2 = 0.1$. Figure 6 displays another combined bright-singular wave configuration. In this figure, the three-dimensional surface exhibits a considerably elevated plateau separated from the surrounding regions by a sharp transition. The amplitude variation is more pronounced than that observed in some of the preceding figures, indicating the strong influence of the selected parameter values on the wave intensity. The corresponding contour plot reveals a central region of relatively high amplitude bounded by regions of lower amplitude. The relatively uniform structure of the central region suggests that the wave maintains a clearly defined profile over the displayed domain. The comparison between Figures 5 and 6 demonstrates how different parameter combinations can produce substantial changes in the amplitude and spatial distribution of nonlinear wave solutions.

Figure 4 displays a singular periodic wave solution when $h = 0.001, k = 1, \rho = 12, \lambda = 0.1, \sigma = 0.1, P = 0.5, W = 1.2, \alpha = 0.5, \beta = 1, \gamma_0 = 0.5, \rho_0 = 0.005, \delta_1 = 1, \delta_2 = 0.1$. Figure 7 presents a singular periodic wave solution. Unlike the localized profiles observed in the preceding figures, the three-dimensional surface exhibits a periodically varying structure with sharp amplitude transitions. The contour representation reveals distinct parallel bands, indicating the repetitive spatial organization of the wave profile. The periodic arrangement of these contours reflects the oscillatory nature of the underlying trigonometric solution family. The presence of singular features distinguishes this solution from a conventional smooth periodic wave. This graphical behaviour demonstrates the ability of the proposed method to generate periodic structures with singular characteristics, which may be useful in describing complex wave patterns in nonlinear telecommunication systems.



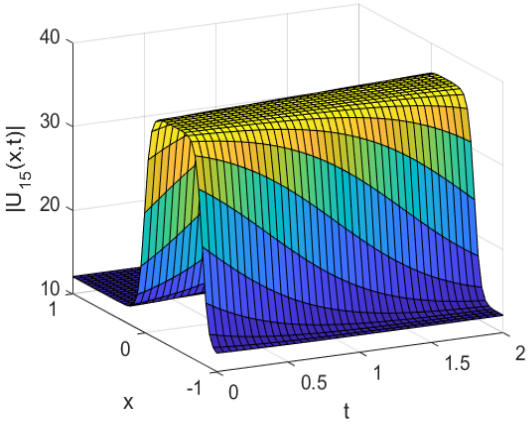
(a)



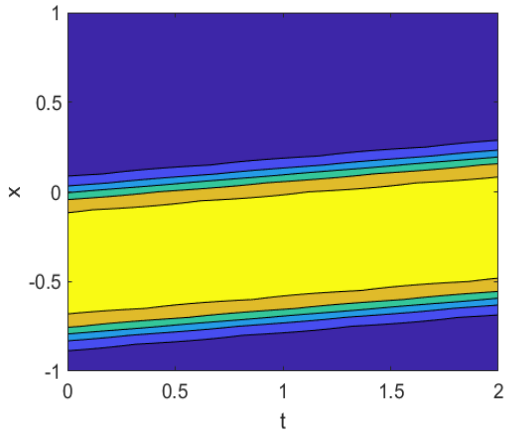
(b)

Fig. 4: 3-D (a) and contour (b) visualization of $|U_{13}(x,y,t)|$.

© 2027 NSP
Natural Sciences Publishing Cor.



(a)

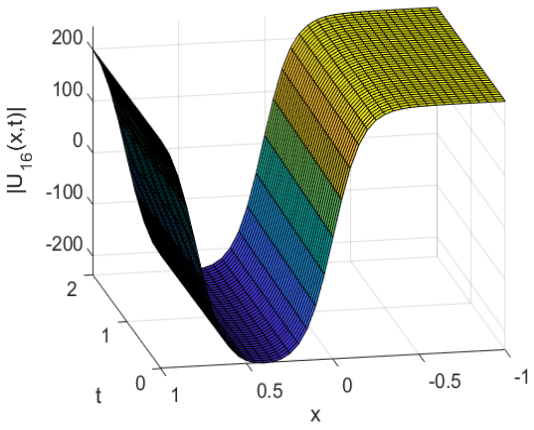


(b)

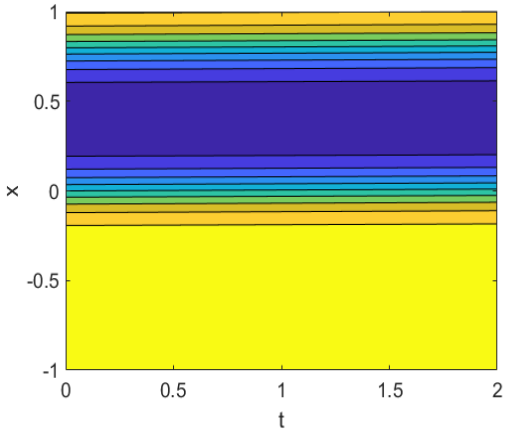
Fig. 5: 3-D (a) and contour (b) visualization of $|U_{15}(x,y,t)|$.

Figure 5 displays a combo periodic wave solution when $h = 0.1, k = 1, \rho = 12, \lambda = 0.1, \sigma = 0.1, P = 0.5, W = 1.2, \alpha = 0.5, \beta = 1, \gamma_0 = 0.5, \rho_0 = 0.005, \delta_1 = 1, \delta_2 = 0.1$. Figure 8 illustrates a combination of periodic wave structures. The three-dimensional surface exhibits a broad, relatively elevated region bounded by sharp transitions, while the contour plot displays a series of parallel bands extending across the considered domain. These features indicate a periodic spatial organization of the solution, with distinguishable regions of different amplitudes. Compared with Figure 7, the graphical structure exhibits a more regular and smoother distribution across the spatial domain. This difference emphasizes the role of the solution parameters in determining whether the resulting periodic structures exhibit singular behaviour or relatively regular wave profiles. The figure therefore provides further evidence of the diversity of nonlinear periodic solutions supported by the telecommunication model.

Figure 6 displays a singular periodic wave solution when $h = 0.005, k = 1, \rho = 12, \lambda = 0.1, \sigma = 0.1, P = 0.5, W = 1.2, \alpha = 0.5, \beta = 1, \gamma_0 = 0.5, \rho_0 = 0.005, \delta_1 = 1, \delta_2 = 0.1$. Figure 9 presents a singular periodic wave solution characterized by a pronounced variation in amplitude. The three-dimensional surface displays a localized depression followed by a steep transition toward a region of higher amplitude. This configuration produces a distinctive wave profile with strong spatial variations. The corresponding contour plot consists of nearly horizontal bands separated by relatively narrow transition regions, indicating that the principal amplitude changes occur across specific spatial locations. The graphical representation confirms the coexistence of periodic and singular characteristics in the analytical solution. It also illustrates how the selected parameters influence the spatial localization and intensity of the resulting wave structure.



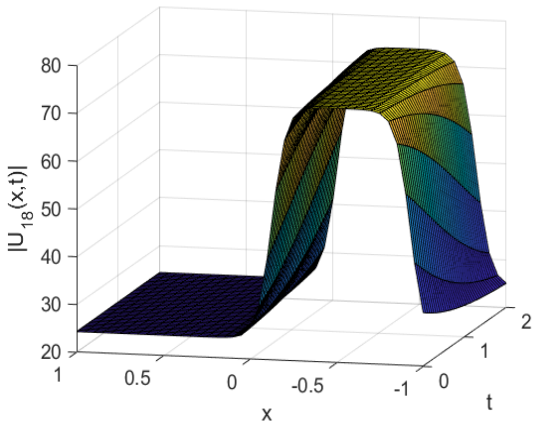
(a)



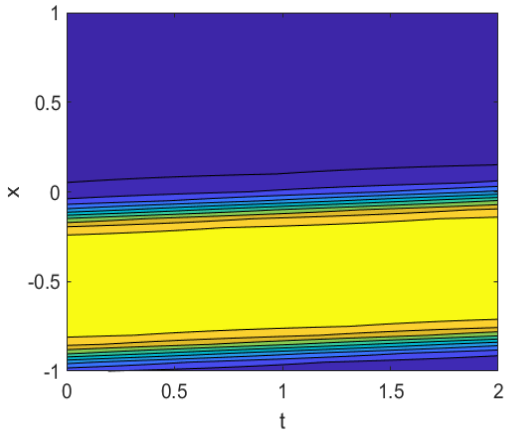
(b)

Fig. 6: 3-D (a) and contour (b) visualization of $|U_{16}(x,y,t)|$.

© 2027 NSP
Natural Sciences Publishing Cor.



(a)

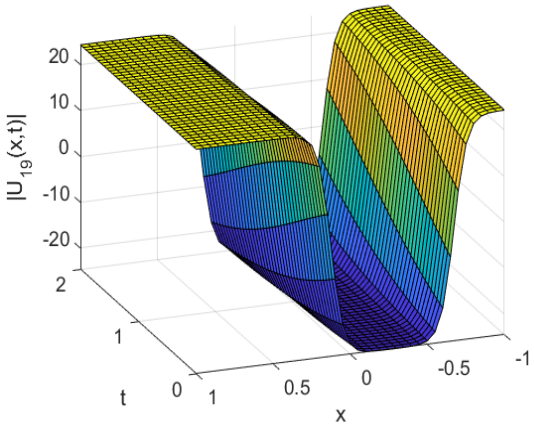


(b)

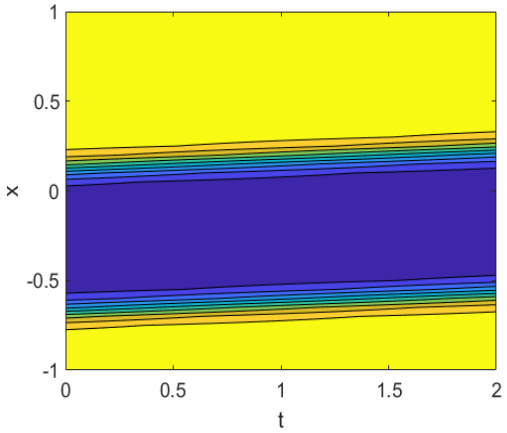
Fig. 7: 3-D (a) and contour (b) visualization of $|U_{18}(x,y,t)|$.

Figure 7 displays a combo periodic wave solution when $h = 0.05, k = 1, \rho = 12, \lambda = 0.1, \sigma = 0.1, P = 0.5, W = 1.2, \alpha = 0.5, \beta = 1, \gamma_0 = 0.5, \rho_0 = 0.005, \delta_1 = 1, \delta_2 = 0.1$. Figure 10 demonstrates another combination of periodic wave structures. The three-dimensional surface exhibits a localized elevated region with relatively sharp boundaries, while the contour plot shows a well-defined band extending across the spatial domain. The comparatively smooth distribution of the contours indicates a more regular propagation pattern than that observed in the singular periodic configurations. The wave profile maintains distinguishable amplitude regions throughout the considered interval, illustrating the capacity of the governing equation to support periodic wave structures with different geometrical characteristics. The comparison with Figure 9 further demonstrates the influence of the solution parameters on the formation and configuration of periodic waves.

Figure 8 displays a combo periodic wave solution when $h = 0.05, k = 1, \rho = 12, \lambda = 0.1, \sigma = 0.1, P = 0.5, W = 1.2, \alpha = 0.5, \beta = 1, \gamma_0 = 0.5, \rho_0 = 0.005, \delta_1 = 1, \delta_2 = 0.1$. Figure 11 illustrates a combination of periodic wave structures with pronounced amplitude variations. The three-dimensional surface displays multiple elevated and depressed regions, producing a more complicated wave configuration than those observed in Figures 8 and 10. The contour representation reveals distinct parallel bands that correspond to the different amplitude regions of the solution. The presence of multiple transitions indicates a complex spatial organization of the wave profile. These features demonstrate that the nonlinear telecommunication equation can support more than one type of periodic wave configuration, depending on the selected parameters and the corresponding Riccati solution family.



(a)



(b)

Fig. 8: 3-D (a) and contour (b) visualization of $|U_{19}(x,y,t)|$.

© 2027 NSP
Natural Sciences Publishing Cor.

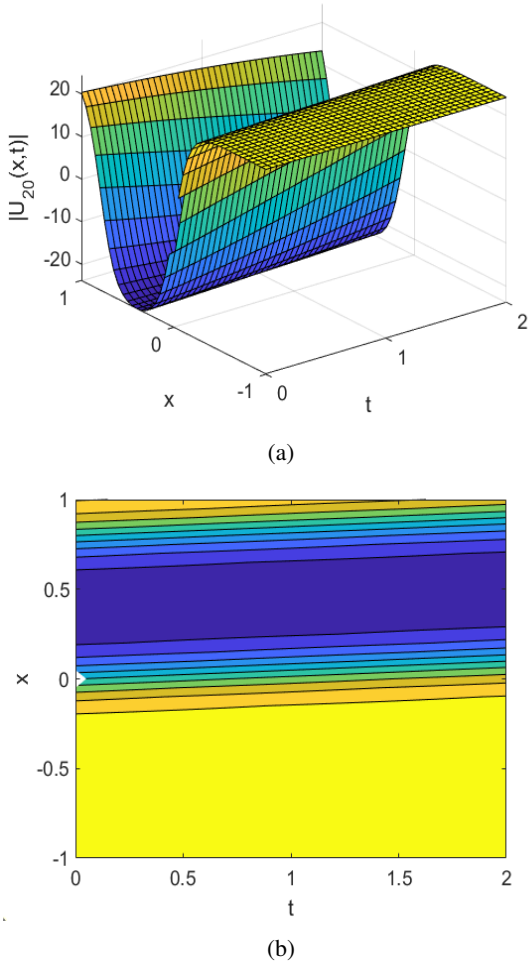


Fig. 9: 3-D (a) and contour (b) visualization of $|U_{20}(x,y,t)|$.

Figure 9 displays a periodic wave solution when $h = 0.05, k = 1, \rho = 12, \lambda = 0.1, \sigma = 0.1, P = 0.5, W = 1.2, \alpha = 0.5, \beta = 1, \gamma_0 = 0.5, \rho_0 = 0.005, \delta_1 = 1, \delta_2 = 0.1$. Figure 12 represents a periodic wave solution characterized by a relatively regular distribution of its amplitude. The three-dimensional surface exhibits a sequence of elevated and depressed regions extending along the propagation direction. The corresponding contour plot reveals a set of parallel bands with gradual variations in their spatial arrangement. Compared with the more complicated configuration in Figure 11, this solution exhibits a comparatively uniform periodic structure. This behaviour highlights the ability of the proposed analytical approach to generate both complex periodic configurations and relatively regular wave patterns. Such diversity is important for understanding the different propagation regimes that can arise in nonlinear telecommunication models.

Figure 10 displays a combo periodic wave solution when $h = 0.05, k = 1, \rho = 12, \lambda = 0.1, \sigma = 0.1, P = 0.5, W = 1.2, \alpha = 0.5, \beta = 1, \gamma_0 = 0.5, \rho_0 = 0.005, \delta_1 = 1, \delta_2 = 0.1$. Figure 13 depicts a combination of periodic wave structures with distinct amplitude transitions. The three-dimensional representation shows a localized depression accompanied by an elevated region, while the contour plot reveals several well-defined parallel bands. The sharp boundaries between these regions indicate substantial spatial variations in the wave amplitude. The overall configuration demonstrates that the nonlinear interaction terms in the governing equation can generate periodic structures with different amplitude levels and geometrical profiles. This figure, together with Figures 7–12, confirms the richness of the periodic solution family obtained through the extended generalized Riccati equation mapping method.

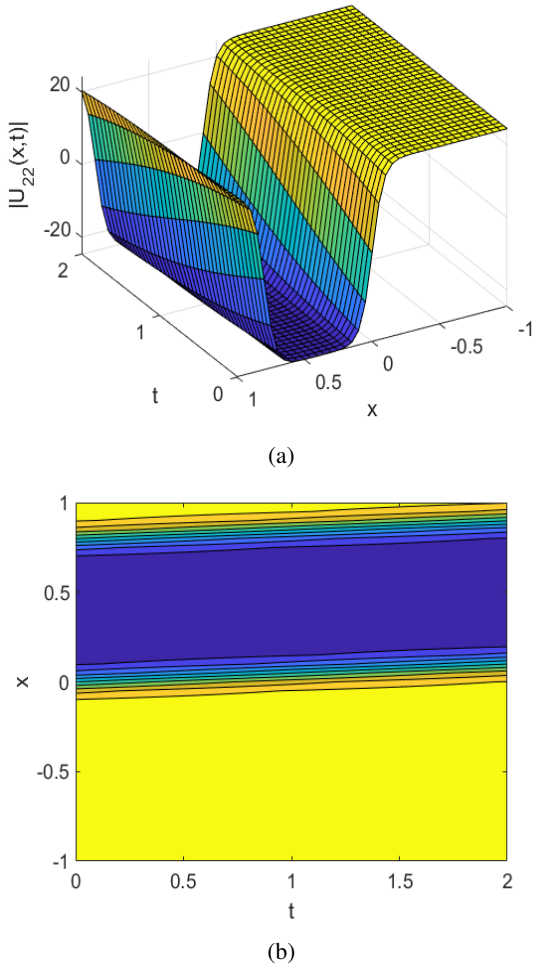
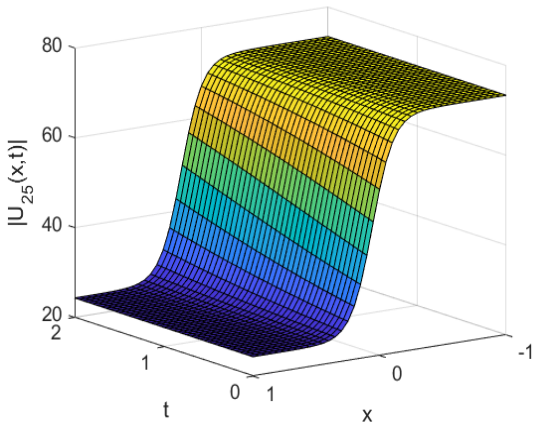
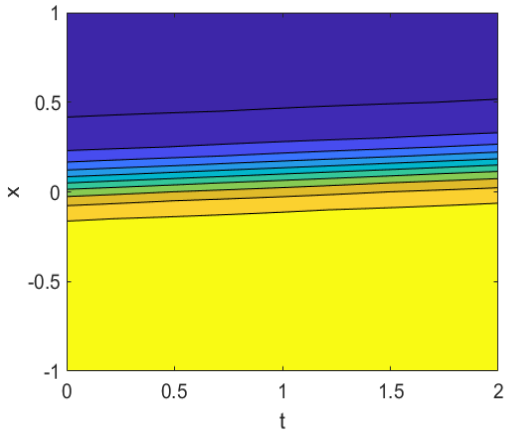


Fig. 10: 3-D (a) and contour (b) visualization of $|U_{22}(x,y,t)|$.

© 2027 NSP
Natural Sciences Publishing Cor.



(a)

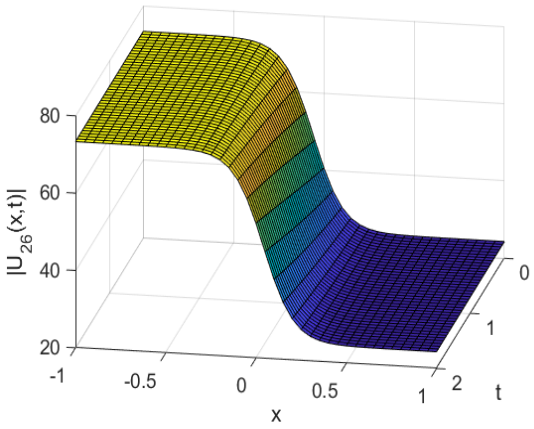


(b)

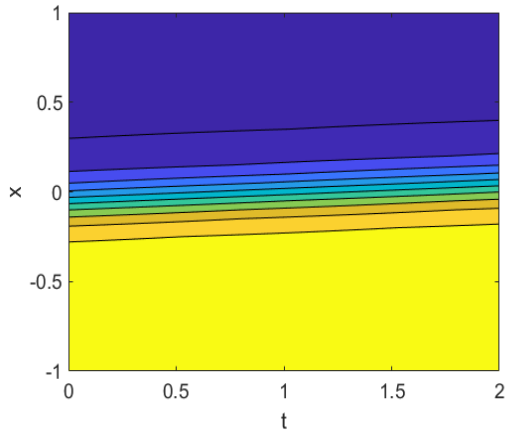
Fig. 11: 3-D (a) and contour (b) visualization of $|U_{25}(x,y,t)|$.

Figure 11 displays a singular soliton wave solution when $h = 0.05, k = 1, \rho = 12, \lambda = 0.1, \sigma = 0.1, P = 0.5, W = 1.2, \alpha = 0.5, \beta = 1, \gamma_0 = 0.5, \rho_0 = 0.005, \delta_1 = 1, \delta_2 = 0.1$. Figure 14 illustrates a singular soliton solution characterized by a pronounced localized transition between regions of different amplitudes. The three-dimensional surface exhibits a relatively elevated wave region separated from the surrounding lower-amplitude region by a steep transition. The contour representation shows a clearly defined boundary between these regions, indicating a localized variation in the wave profile. Unlike the periodic structures presented in the previous figures, the solution exhibits a more localized soliton-type configuration. This behaviour emphasizes the ability of the telecommunication model to describe singular wave structures in addition to periodic and combined wave patterns.

Figure 12 displays a singular soliton wave solution when $h = 0.05, k = 1, \rho = 12, \lambda = 0.1, \sigma = 0.1, P = 0.5, W = 1.2, \alpha = 0.5, \beta = 1, \gamma_0 = 0.5, \rho_0 = 0.005, f_1 = 0.5, \delta_1 = 1, \delta_2 = 0.1$. Figure 15 presents another singular soliton solution with a relatively smooth transition between two distinct amplitude regions. The three-dimensional surface reveals a characteristic descending wave profile, connecting a region of higher amplitude to a region of lower amplitude. The corresponding contour plot displays approximately parallel bands with gradual spatial displacement. Compared with Figure 14, the wave profile exhibits a different orientation and amplitude distribution, demonstrating the influence of the parameters on the geometrical characteristics of the singular soliton. The figure further illustrates the flexibility of the analytical solutions in describing different forms of localized nonlinear wave propagation.



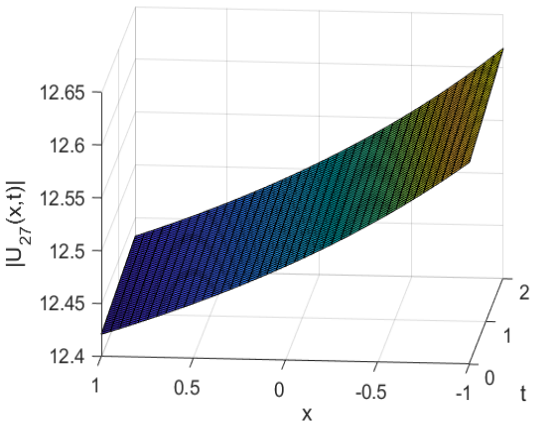
(a)



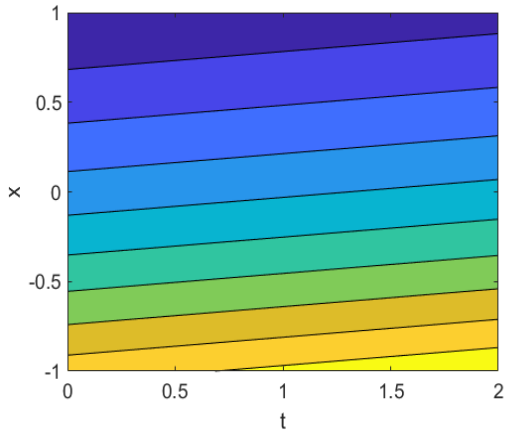
(b)

Fig. 12: 3-D (a) and contour (b) visualization of $|U_{26}(x,y,t)|$.

© 2027 NSP
Natural Sciences Publishing Cor.



(a)



(b)

Fig. 13: 3-D (a) and contour (b) visualization of $|U_{27}(x,y,t)|$.

Figure 13 displays a rational wave solution when $h = 0.1, k = 1, \rho = 12, \lambda = 0.1, \sigma = 0.1, P = 0.5, W = 1.2, \alpha = 0.5, \beta = 1, \gamma_0 = 0.5, \rho_0 = 0.005, l_1 = 0.5, \delta_1 = 1, \delta_2 = 0.1$. Figure 16 illustrates a rational wave solution, which differs from the hyperbolic and trigonometric structures observed in the preceding figures. The three-dimensional surface exhibits a relatively smooth and gradual variation in amplitude across the spatial domain, without the pronounced localized peaks or oscillatory patterns associated with the other solution families. The corresponding contour plot displays smooth, nearly parallel curves, indicating a continuous variation in the wave amplitude. This behaviour is consistent with the rational functional structure of the analytical solution obtained under the corresponding parameter restrictions. The figure demonstrates that the proposed method is capable of generating not only soliton and periodic solutions but also rational wave structures, thereby extending the range of possible analytical descriptions of the nonlinear telecommunication equation.

The obtained solutions include bright-dark combinations, bright-singular combinations, singular solitons, singular periodic waves, periodic waves, and rational structures. The three-dimensional representations provide a clear illustration of the amplitude distribution and geometrical configuration of each solution, whereas the contour plots offer complementary information about the spatial organization and propagation characteristics of the corresponding wave profiles.

An important observation is that the geometrical characteristics of the obtained solutions depend strongly on the parameters appearing in the governing equation and the generalized Riccati equation. Variations in these parameters can modify the wave amplitude, the sharpness of the transitions, the spatial localization, and the overall configuration of the wave structures. In particular, the discriminant condition

$$(\rho^2 - 4\lambda\sigma)$$

determines the nature of the auxiliary Riccati solutions and consequently distinguishes between hyperbolic-type and trigonometric-type solution families. The special parameter cases also produce additional solution structures, including exponential-type and rational solutions.

From the perspective of nonlinear telecommunication systems, these analytical structures provide useful mathematical representations of different possible signal profiles in nonlinear transmission media. Bright and dark soliton structures describe localized variations in signal amplitude, whereas periodic solutions represent spatially repetitive wave patterns. Singular solutions illustrate configurations involving strong amplitude variations and mathematical singularities, while rational solutions provide smooth, nonperiodic amplitude distributions. Nevertheless, the singular profiles require particular care in physical interpretation because their mathematical singularities may restrict their direct applicability to practical transmission systems.

Finally, the graphical agreement between the three-dimensional surfaces and their corresponding contour representations supports the consistency of the obtained analytical expressions. The results collectively demonstrate the effectiveness of the extended generalized Riccati equation mapping method in constructing a broad range of exact solutions to nonlinear partial differential equations. They also highlight the important role of the model parameters in controlling the geometrical properties of nonlinear waves and provide a foundation for further investigations of nonlinear signal propagation in telecommunication networks.

6 Physical interpretation

In order to demonstrate the physical behavior of the provided solutions and to define the shape of the solitary

© 2027 NSP
Natural Sciences Publishing Cor.

wave solutions, this part illustrates the obtained solutions using 3-D and contour graphs. Information regarding the structure and three-dimensional propagation of a single wave can be obtained from 3-D plots. Numerous characteristics of solitary waves, including their amplitude, propagation direction, shape and speed, can be shown in 3-D charts. They can also illustrate the complicated dynamics of wave breaking and dispersion by displaying the wave's interactions in three dimensions with barriers or boundaries. Contour plots are a helpful resource for studying and evaluating solitary waves, as they offer a comprehensive and quantitative depiction of their features and behavior. They are helpful in establishing the presence of solitons, nonlinear effects, and other important wave function properties.

The study of nonlinear telecommunication models is closely related to broader investigations of nonlinear wave propagation, optical interactions, and dynamical phenomena in mathematical physics. Previous studies have extensively investigated nonlinear effects in quantum-optical systems, particularly the Jaynes–Cummings model, where entropic uncertainty, quantum entanglement, quasiprobability distributions, and entropy squeezing provide important insights into the behavior of interacting systems [1]- [10]. Furthermore, investigations of Kerr nonlinearity and nonlinear optical fields have demonstrated the significant influence of nonlinear media on the evolution and phase properties of optical systems [9]. These studies provide complementary theoretical foundations for understanding nonlinear interactions and their implications for optical communication. From another perspective, the stability of nonlinear dynamical systems has been addressed through Lyapunov theory, offering useful mathematical insights into the analysis of dynamical behaviour and stability properties [4].

More directly, recent research has explored soliton solutions of higher-dimensional nonlinear evolution equations using different analytical techniques, demonstrating the importance of exact solutions in describing complex wave propagation phenomena [6]. Motivated by these developments, the present work investigates the $(2+1)$-dimensional nonlinear telecommunication equation using the extended generalized Riccati equation mapping method, yielding various classes of exact solutions, including bright, dark, singular, periodic, and rational waves. Consequently, the present investigation contributes to the broader understanding of nonlinear wave dynamics and provides additional analytical descriptions of wave propagation in nonlinear telecommunication systems, particularly in the context of optical fiber communication.

7 Discussion and conclusion

In this work, we have demonstrated that the soliton solutions of nonlinear electrical transmission lines may be constructed using the extended generalized Riccati equation mapping method. In order to observe how some of these solutions change across time and space, we have plotted them using appropriate parameter settings. It is evident that the current work contains numerous new solutions when we contrast our findings with those found in [26, 28, 29]. Our novel method might be very useful in communication networks where data is transmitted via soliton technology. Certain solutions have been explained physically. The fact that other nonlinear equations in mathematical physics can be solved using the same methodology makes this work even more interesting. We have plotted these solutions and demonstrated that controlling the network's parameters may change the geometry of the solutions.

References

[1] Roshid, M. M., & Roshid, H. O. (2018). Exact and explicit traveling wave solutions to two nonlinear evolution equations which describe incompressible viscoelastic Kelvin-Voigt fluid. Heliyon, 4(8).

[2] Khatun, M. S., Hoque, M. F., & Rahman, M. A. (2020). A class of localized soliton and fractal pattern solutions of the (2+ 1)-dimensional modified dispersive long wave model. Physica Scripta, 95(8), 085219.

[3] Ouyang, Y., Dong, L., Xue, L., & Sun, C. (2019). Adaptive control based on neural networks for an uncertain 2-DOF helicopter system with input deadzone and output constraints. IEEE/CAA Journal of Automatica Sinica, 6(3), 807-815.

[4] Kumar, A., Ilhan, E., Ciancio, A., Yel, G., & Baskonuş, H. M. (2021). Extractions of some new travelling wave solutions to the conformable Date-Jimbo-Kashiwara-Miwa equation.

[5] Ali, K. K., & Mehanna, M. S. (2021). Traveling wave solutions and numerical solutions of Gilson–Pickering equation. Results in Physics, 28, 104596.

[6] Abdeljabbar, A., & Tran, T. D. (2016). Pfaffian solutions to a generalized KP system with variable coefficients. Appl. Math. Sci, 10(48), 2351-2368.

[7] Yusuf, A., Sulaiman, T. A., Abdeljabbar, A., & Alquran, M. (2023). Breather waves, analytical solutions and conservation laws using Lie–Bäcklund symmetries to the (2+ 1)-dimensional Chaffee–Infante equation. Journal of Ocean Engineering and Science, 8(2), 145-151.

[8] Khatun, M. S., Akter, S., & Roshid, M. M. (2020). Novel localized excitations structures with fusion and fission properties to a (2+ 1)-dimensional breaking soliton equation. International Journal of Applied and Computational Mathematics, 6, 1-12.

[9] Ullah, M. S., Roshid, H. O., & Ali, M. Z. (2024). New wave behaviors and stability analysis for the (2+ 1)-dimensional Zoomeron model. Optical and Quantum Electronics, 56(2), 240.

[10] Tala-Tebue, E., & Zayed, E. M. E. (2018). New Jacobi elliptic function solutions, solitons and other solutions for the (2+ 1)-dimensional nonlinear electrical transmission line equation. The European Physical Journal Plus, 133, 1-7.

© 2027 NSP
Natural Sciences Publishing Cor.

[11] Baskonus, H. M., Cattani, C.,& Ciancio, A. (2019). Periodic, complex and kink-type solitons for the nonlinear model in microtubules. Appl. Sci, 21, 34-45.
[12] Rahman, N., & Akbar, M. A. (2013). Traveling waves solutions of nonlinear Klein Gordon equation by extended (G′/G)-expansion method. Annals of Pure and Applied Mathematics, 3(1), 10-16.
[13] Abdeljabbar, A. (2021). New double Wronskian exact solutions for a generalized (2+ 1)-dimensional nonlinear system with variable coefficients. Partial Differential Equations in Applied Mathematics, 3, 100022.
[14] Sulaiman, T. A., Yusuf, A., Abdeljabbar, A., & Alquran, M. (2021). Dynamics of lump collision phenomena to the (3+ 1)-dimensional nonlinear evolution equation. Journal of Geometry and Physics, 169, 104347.
[15] Kirane, M., & Abdeljabbar, A. (2022). Nonexistence of global solutions of systems of time fractional differential equations posed on the Heisenberg group. Mathematical Methods in the Applied Sciences, 45(12), 7336-7345.
[16] Islam, Z., Sheikh, M. A. N., Roshid, H. O., Hossain, M. A., Taher, M. A., & Abdeljabbar, A. (2024). Stability and spin solitonic dynamics of the HFSC model: effects of neighboring interactions and crystal field anisotropy parameters. Optical and Quantum Electronics, 56(2), 190.
[17] Yel, G., & Aktürk, T. (2020). A new approach to (3+ 1) dimensional Boiti–Leon–Manna–Pempinelli equation. Applied Mathematics and Nonlinear Sciences, 5(1), 309-316.
[18] Özer, Ö. (2019). A handy technique for fundamental unit in specific type of real quadratic fields. Applied Mathematics and Nonlinear Sciences, 5(1), 495-498.
[19] Cordero, A., Jaiswal, J. P., & Torregrosa, J. R. (2019). Stability analysis of fourth-order iterative method for finding multiple roots of non-linear equations. Applied Mathematics and Nonlinear Sciences, 4(1), 43-56.
[20] Rahman, M. A. (2014). The $\exp(-\Phi(\eta))$-expansion method with application in the (1+ 1)-dimensional classical Boussinesq equations. Results in Physics, 4, 150-155.
[21] Akgandüller, Ö., & Atmaca, S. P. (2020). Discrete normal vector field approximation via time scale calculus. Applied Mathematics and Nonlinear Sciences, 5(1), 349-360.
[22] Rahman, N., & Akbar, M. A. (2013). Traveling waves solutions of nonlinear Klein Gordon equation by extended (G′/G)-expansion method. Annals of Pure and Applied Mathematics, 3(1), 10-16.
[23] Ullah, A., Ullah, Z., Abdeljawad, T., Hammouch, Z., & Shah, K. (2021). A hybrid method for solving fuzzy Volterra integral equations of separable type kernels. Journal of King Saud University-Science, 33(1), 101246.
[24] Li, Y. M., Rashid, S., Hammouch, Z., Baleanu, D., & Chu, Y. M. (2021). New Newton's type estimates pertaining to local fractional integral via generalized p-convexity with applications. Fractals, 29(05), 2140018.
[25] Ali, A. R., Islam, S., & Khatun, A. (2023). Wave solutions of nonlinear model occurs in telecommunications.
[26] Baskonus, H. M., Guirao, J. L. G., Kumar, A., Vidal Causanilles, F. S., & Bermudez, G. R. (2021). Regarding new traveling wave solutions for the mathematical model arising in telecommunications. Advances in Mathematical Physics, 2021, 1-11.
[27] Kumar, H., & El-Ganaini, S. (2020). Traveling and localized solitary wave solutions of the nonlinear electrical transmission line model equation. The European Physical Journal Plus, 135(9), 1-25.
[28] Tala-Tebue, E., & Zayed, E. M. E. (2018). New Jacobi elliptic function solutions, solitons and other solutions for the (2+ 1)-dimensional nonlinear electrical transmission line equation. The European Physical Journal Plus, 133, 1-7.
[29] Sardar, A., Husnine, S. M., Rizvi, S. T. R., Younis, M.,& Ali, K. (2015). Multiple travelling wave solutions for electrical transmission line model. Nonlinear Dynamics, 82, 1317-1324.
[30] Naher, H., & Abdullah, F. A. (2012). New traveling wave solutions by the extended generalized Riccati equation mapping method of the-dimensional evolution equation. Journal of Applied Mathematics, 2012.
[31] Naher, H., Abdullah, F. A., & Mohyud-Din, S. T. (2013). Extended generalized Riccati equation mapping method for the fifth-order Sawada-Kotera equation. AIP Advances, 3(5).
[32] Naher, H., & Abdullah, F. A. (2012). The modified Benjamin-Bona-Mahony equation via the extended generalized Riccati equation mapping method. Applied Mathematical Sciences, 6(111), 5495-5512.
[33] Sebawe Abdalla, M., Hassan, S.S., Abdel-Aty, M. (2005). Entropic uncertainty in the Jaynes-Cummings model in presence of a second harmonic generation, Optics Communications, 2005, 244(1-6), pp. 431–443 DOI: http://dx.doi.org/10.1016/j.optcom.2004.09.051
[34] Abdel-Aty, M. (2003). An investigation of entanglement and quasiprobability distribution in a generalized Jaynes-Cummings model, Journal of Mathematical Physics, 44(4), pp. 1457–1471 DOI: http://dx.doi.org/10.1063/1.1559643
[35] Abdel-Aty, M., Sebawe Abdalla, M., Obada, A.-S.F. (2002). Entropy squeezing of a two-mode multiphoton Jaynes-Cummings model in the presence of a nonlinear medium, Journal of Optics B Quantum and Semiclassical Optics, 4(2), pp. 134–142 DOI: http://dx.doi.org/10.1088/1464-4266/4/2/309
[36] Wang, Zengyun,Cao, Jinde,Cai, Zuowei,Abdel-Aty, Mahmoud A. (2020) A novel Lyapunov theorem on finite/fixed-time stability of discontinuous impulsive systems, Chaos, 30(1), 013139 DOI: http://dx.doi.org/10.1063/1.5121246
[37] Abdel-Aty, M., Abdel-Khalek, S., Obada, A.-S.F. (2000). Pancharatnam phase of two-mode optical fields with Kerr nonlinearity, Optical Review, 7(6), pp. 499–504 DOI: http://dx.doi.org/10.1007/s10043-000-0499-6
[38] Rehman, H.U., Said, G.S., Amer, A., Elazab, N.S., Osman, M.S. (2024). Unraveling the (4+1)-dimensional Davey-Stewartson-Kadomtsev-Petviashvili equation: Exploring soliton solutions via multiple techniques, Alexandria Engineering Journal, 90, pp. 17–23 DOI: http://dx.doi.org/10.1016/j.aej.2024.01.058
[39] Abdel-aty, M. (2003). Quantum field entropy and entanglement of a three-level atom two-mode system with an arbitrary nonlinear medium, Journal of Modern Optics, 50(2), pp. 161–177 DOI: http://dx.doi.org/10.1080/09500340308235167
[40] El-Shahat, T.M., Abdel-Khalek, S., Abdel-Aty, M., Obada, A.-S.F. (2003). Aspects on entropy squeezing

© 2027 NSP
Natural Sciences Publishing Cor.

of a two-level atom in a squeezed vacuum, Chaos Solitons and Fractals, 2003, 18(2), pp. 289–298 DOI: http://dx.doi.org/10.1016/S0960-0779(02)00652-5

[41] Obada, A.-S.F., Abdel-Aty, M. (2000). Influence of the stark shift and kerr-like medium on the evolution of field entropy and entanglement in two-photon processes, Acta Physica Polonica B, 31(3), pp. 589–599

[42] Abdel-Aty, M., Abdalla, M.S., Obada, A.-S.F. (2002). Entropy and phase properties of isotropic coupled oscillators interacting with a single atom: one- and two-photon processes, Journal of Optics B Quantum and Semiclassical Optics, 4(3), pp. S133–S141 DOI: http://dx.doi.org/10.1088/1464-4266/4/3/367

[43] Zhang, J.-S., Chen, A.-X., Abdel-Aty, M. (2010). Two atoms in dissipative cavities in dispersive limit: Entanglement sudden death and long-lived entanglement, Journal of Physics B Atomic Molecular and Optical Physics, 43(2), 025501 DOI: http://dx.doi.org/10.1088/0953-4075/43/2/025501

© 2027 NSP
Natural Sciences Publishing Cor.